Wearable magnetoencephalography in a lightly shielded environment

Niall Holmes*, James Leggett, Ryan M. Hill, Lukas Rier, Elena Boto, Holly Schofield, Tyler Hayward, Eliot Dawson, David Woolger, Vishal Shah, Samu Taulu, Matthew J. Brookes and Richard Bowtell

***Abstract*— Wearable magnetoencephalography based on optically pumped magnetometers (OPM-MEG) offers non-invasive and high-fidelity measurement of human brain electrophysiology. The flexibility of OPM-MEG also means it can be deployed in participants of all ages and permits scanning during movement. However, the magnetic fields generated by neuronal currents – which form the basis of the OPM-MEG signal – are much smaller than environmental fields, and this means measurements are highly sensitive to interference. Further, OPMs have a low dynamic range, and should be operated in near-zero background field. Scanners must therefore be housed in specialised magnetically shielded rooms (MSRs), formed from multiple layers of shielding material. The MSR is a critical component, and current OPM-optimised shields are large (>3 m in height), heavy (>10,000 kg) and expensive (with up to 5 layers of material). This restricts the uptake of OPM-MEG technology. Here, we show that the application of the Maxwell filtering techniques signal space separation (SSS) and its spatiotemporal extension (tSSS) to OPM-MEG data can isolate small signals of interest measured in the presence of large interference. We compare phantom recordings and MEG data from a participant performing a motor task in a state-of-the-art 5-layer MSR, to similar data collected in a lightly shielded room: application of tSSS to data recorded in the lightly shielded room allowed accurate localisation of a dipole source in the phantom and neuronal sources in the brain. Our results point to future deployment of OPM-MEG in lighter, cheaper and easier-to-site MSRs which could catalyse widespread adoption of the technology.**

***Index Terms*— Magnetoencephalography, Magnetic Shielding, Optically pumped magnetometers.**

I. Introduction

Magnetoencephalography (MEG) is a non-invasive functional brain imaging technique, which employs an array of sensitive detectors to measure magnetic fields generated by neuronal currents [1]. The neuronal sources of the measured fields are identified via a 'source reconstruction' process to obtain dynamic 3D images of brain activity with high spatiotemporal resolution. MEG is a powerful tool, offering advantages over techniques such as functional magnetic resonance imaging (fMRI, which cannot directly measure electrophysiology) and electroencephalography (EEG, which has poor spatial precision due to distortion of electric potentials by the skull). MEG has significant application in neuroscience [2] and offers clinical insight in conditions such as epilepsy [3].

Despite its capabilities, MEG has not yet been widely deployed. At the time of writing, we estimate there are only c.200 MEG systems worldwide. Key barriers arise from the significant physics and engineering challenges involved in constructing a system. Neuromagnetic fields are small (~100-1,000 fT), meaning highly sensitive instruments are needed to detect them. Current systems use arrays of superconducting quantum interference devices (SQUIDs), which require cooling to liquid helium temperatures (4 K) to operate. In addition, systems must be housed inside a magnetically shielded room (MSR) to reduce the effects of magnetic interference. Such rooms are constructed by enclosing the array inside several layers of a material with a high magnetic permeability (e.g., nickel-iron alloys such as MuMetal or Permalloy) to shield against static and slowly changing fields, along with a layer of material with a high electrical conductivity (e.g. copper or

This paper was submitted for review on April 8th, 2024. We acknowledge funding from a Medical Research Council Mid-Range Equipment grant (MC_PC_MR/X012263/1) for funding the compact MSR and OPM-MEG system used in this work. We also acknowledge financial support from the UK Quantum Technology Hub in Sensors and Timing (EP/T001046/1) funded by the Engineering and Physical Sciences Research Council (EPSRC). N. Holmes acknowledges financial support of a Mansfield Fellowship funded by the Faculty of Science at the University of Nottingham. S. Taulu acknowledges a National Institutes of Health grant (R21EB033577) as well as the Bezos Family Foundation and the R. B. and Ruth H. Dunn Charitable Foundation for financial support. For the purpose of open access, the author have applied a Creative Commons Attribution (CC BY) license to any Author Accepted Manuscript version arising

N. Holmes is corresponding author for this paper. He is with the Sir Peter Mansfield Imaging Centre, School of Physics and Astronomy, University of Nottingham, University Park, Nottingham, NG7 2RD, U.K. and with Cerca Magnetics Limited, Units 7-8 Castlebridge Office Village, Kirtley Drive, Nottingham, NG7 1LD, U.K. (corresponding e-mail: niall.holmes@nottingham.ac.uk)

J. Leggett, R. M. Hill, L. Rier, E. Boto, H. Schofield, M. J. Brookes and R. Bowtell are with the Sir Peter Mansfield Imaging Centre, School of Physics and Astronomy, University of Nottingham, University Park, Nottingham, NG7 2RD, U.K.

R. M. Hill, E. Boto, H. Schofield, T. Hayward, E. Dawson, D. Woolger, M. J. Brookes and R. Bowtell are with Cerca Magnetics Limited, Units 7-8 Castlebridge Office Village, Kirtley Drive, Nottingham, NG7 1LD, U.K.

D. Woolger is also with Magnetic Shields Limited, Headcorn Road, Staplehurst, Tonbridge, Kent, TN12 0DS, U.K.

V. Shah is with QuSpin Inc., 331 South 104th Street, Suite 130, Louisville, 80027, Colorado, U.S.A.

S. Taulu is with Department of Physics, University of Washington, Seattle, Washington, U.S.A. and with Institute for Learning and Brain Sciences, University of Washington, Seattle, Washington, U.S.A.

aluminium) to shield against higher frequency fields. The cost of shielding, cryogenics, space and infrastructure along with limitations of the final system caused by the fixed sensor array all lead to issues with system deployment. If MEG is to become a widely used technique, both system infrastructure and shielding requirements must be addressed.

Recent years have seen significant research on the use of optically pumped magnetometers (OPMs, see [4], [5] for reviews) for MEG. OPMs are compact devices with magnetic sensitivity comparable to SQUIDs, but without requiring cryogenics. Wearable OPM-MEG systems allow participant movement [6] and can be reconfigured to scan across the lifespan [7]–[9]. It has also been shown to allow ambulatory motion [10], [11] and naturalistic tasks [12]. These significant advantages (over all other neuroimaging techniques) make OPM-MEG an exciting prospect. The commercial availability of systems is also increasing.

However, OPMs do not resolve the challenges of magnetic shielding; instead placing more stringent requirements on the ambient magnetic field. OPMs rely on quantum coherence of spins in a vapour of alkali atoms. To enable the coherent precession of atoms needed to achieve sensitivity to neuromagnetic fields, the atoms must enter the spin exchange relaxation free regime which mitigates spin-exchange collisions that would otherwise decohere the system [13]. This requires the field experienced by the OPM to be zero, meaning MSRs for OPM-MEG must not only shield systems from interference, but also provide a very low static magnetic field environment. This led to the development of 'OPM-optimised' MSRs comprising between 2 and 4 layers of MuMetal, and a single layer of copper. Such MSRs can weigh >10,000 kg, as well as being >3 m in height, leading to siting issues [14]. MSRs are expensive and the cost and installation time scales with the size of the room. For OPM-MEG to realise its full potential, the complexity, and cost of the MSR must be reduced.

Reducing the number of shielding layers reduces size, weight, and cost but leads to a dramatic increase in the amplitude of both the static field and the interference. Nevertheless, there are techniques to mitigate this. For example, demagnetisation coils can be used to reduce the residual magnetisation of the ferromagnetic MuMetal [15]. Additionally, 'active' magnetic shielding with electromagnetic coils can generate magnetic fields which are equal and opposite to residual fields in the MSR [16]–[18]. The signal space separation (SSS) method [19], [20] and its spatiotemporal extension (tSSS) [21] are powerful post-processing techniques that reduce the effect of external magnetic interference. They work by modelling the measured fields as a multipole expansion of solid harmonics, separating signal contributions arising from inside (i.e., the neuronal signals of interest) and outside (interference sources) the sensor array. However, these methods are yet to be applied routinely to OPM-MEG due to a requirement for high channel counts, which until recently [22] have not been available.

In this paper, we construct a unique lightly shielded room with a single complete layer of MuMetal and one layer of copper. We employ active field control to enable a low enough residual field for OPMs to operate, and we contrast recordings made in our light shield to those acquired in a 5-layer OPM-optimised MSR. Empty room noise recordings, 'brain-like' phantom data and real MEG data are all acquired and processed using SSS and tSSS. We aim to show that this combination of hardware and data processing enables signals of interest to be isolated from the background interference in the lighter MSR. We posit that meeting these objectives would be a major step towards widespread deployment of OPM-MEG in cheaper-to-build, and easier-to-site, MSRs.

II. Methods

A. Shielded Rooms

Data were collected in two MSRs, both at the Sir Peter Mansfield Imaging Centre, University of Nottingham, UK.

MSR1 (Fig. 1(a)) is an OPM-optimized design, constructed using four layers of MuMetal (two 1.5 mm thick outer layers placed in contact with each other, two 1 mm thick inner layers also in contact) and one 6 mm thick layer of copper (between MuMetal layers) (MuRoom, Magnetic Shields Limited, Kent, UK). It has an internal footprint of 3 x 3 m^2 with height 2.3 m. The walls are ~0.5 m thick, meaning an external footprint of 3.7 x 4.0 m^2 and height of 3.4 m. The MSR weighs c.12,000 kg. This MSR incorporates demagnetization coils which reduce the remanent magnetic field to ~2 nT [15]. The surrounding area experiences minimal magnetic disturbances with temporal field drift ~100 pT/min [23]. The empty room OPM sensor noise is <20 fT/√Hz 1-100 Hz.

MSR2 (Fig.1(b-c)) is a partially constructed MSR (Compact MuRoom, Cerca Magnetics Limited, Nottingham, UK). At the point construction was paused for these experiments, the room featured one complete layer of 1.5 mm thick MuMetal (innermost layer), one complete layer of 4 mm thick copper, and a partially completed (one vertical wall and the floor) outermost MuMetal layer. No degaussing coils were available for our experiments. The internal footprint is 1.3 x 1.3 m^2 with height 2.0 m. The external dimensions are 1.6 x 1.6 x 2.4 m^3 and the MSR weighs c.2,000 kg. The residual field magnitude measured by a fluxgate magnetometer (SENSYS, Bad Saarow, Germany) was >100 nT, with temporal drifts ~1 nT/min.

Fig. 1. Magnetically shielded rooms. Two MSRs were used with varying levels of shielding. (a) MSR1: An OPM-optimised, 5-layer (4-layers of MuMetal and 1 layer of copper) MSR with a external footprint of 3.7 x 4.0 m^2 and height of 3.4 m. (b) MSR2: A partially constructed compact MSR with one complete layer of MuMetal and one layer of copper. The external footprint is 1.6 x 1.6 m^2 and the height is 2.4 m. The environmental interference is greater in MSR2, but it is cheaper and easier to site. (c) A participant seated inside MSR2 wearing an OPM-MEG helmet. The wooden structure is an electromagnetic coil which is used to cancel the background magnetic field to enable OPM operation.

B. OPM-MEG system

The OPMs used for all experiments were third generation triaxial QuSpin Zero Field Magnetometers controlled by an integrated miniaturized electronics system (ZFM with Neuro-1-electronics, QuSpin Inc., Louisville, Colorado, USA) as described by Schofield et al. [24]. The sensors have a noise floor of <15 fT/√Hz between 1-100 Hz. 64 OPMs (i.e. 192-channels) were mounted into a generic 3D-printed helmet (Cerca) which provides approximately whole-head coverage of an adult participant [22]. All data were sampled at 375 Hz. In this system, the triaxial on-sensor electromagnetic coils can cancel static fields up to 50 nT to facilitate sensor operation. These sensors have a demonstrated dynamic range of ±8 nT via operation in triaxial 'closed-loop' mode, where feedback of the sensor output in all three directions to the on-sensor coils keeps the cell at zero magnetic field, ensuring linearity and minimizing gain and cross-axis projection errors [25].

C. The signal space separation method

Data collected in MSR2 are likely to contain strong interference. The SSS method is a commonly deployed post-processing tool for analyzing cryogenic MEG data. Briefly, a multipole expansion is used to describe the range of magnetic fields that can be measured by a MEG array (that may consist of SQUID or OPM sensors). By assuming the helmet is free from sources of magnetic field, a magnetic scalar potential can be described using a series expansion of regular and irregular solid harmonic functions as,

$$V(\boldsymbol{r}) = \sum_{l=1}^{\infty}\sum_{m=-l}^{l} \alpha_{lm}\frac{Y_{lm}(\theta,\varphi)}{r^{l+1}} + \sum_{l=1}^{\infty}\sum_{m=-l}^{l} \beta_{lm} r^{l} Y_{lm}(\theta,\varphi) \quad [1]$$

where

$$Y_{lm}(\theta,\varphi) = \sqrt{\frac{2l+1}{4\pi}\frac{(l-m)!}{(l+m)!}} P_{lm}(\cos(\theta)) e^{im\varphi} \quad [2]$$

is the normalized spherical harmonic function which represents spatial oscillations that increase in spatial frequency with increasing values of l (and m); r, θ and φ are spherical polar coordinates; $P_{lm}(\cos(\theta))$ is the associated Legendre function; and α_{lm} and β_{lm} are weighting coefficients. For an origin point inside the helmet, terms proportional to $r^{-(l+1)}$ are singular at the origin and best describe sources that are closer to the origin than the sensors (i.e. the neuronal sources of interest). Terms proportional to r^{l} diverge at infinity and best describe sources that are further from the origin than the sensors (i.e. interference). Signal vectors $\boldsymbol{S}$ measured by the array corresponding to the internal and external subspaces can be calculated for the array geometry and expressed as

$$\boldsymbol{\Phi} = [\boldsymbol{S}_{in}\ \boldsymbol{S}_{out}]\begin{bmatrix}\boldsymbol{x}_{in}\\ \boldsymbol{x}_{out}\end{bmatrix} = \boldsymbol{S}\boldsymbol{x}. \quad [4]$$

To estimate the internal signal ($\widehat{\boldsymbol{\Phi}}_{in}$) from the total measured signal $\boldsymbol{\Phi}$ one can estimate a weights vector ($\widehat{\boldsymbol{x}}$) via the pseudo-inverse $\boldsymbol{S}^{+}$ as

$$\widehat{\boldsymbol{x}} = \begin{bmatrix}\widehat{\boldsymbol{x}}_{in}\\ \widehat{\boldsymbol{x}}_{out}\end{bmatrix} = \boldsymbol{S}^{+}\boldsymbol{\Phi} \quad [5]$$

followed by computation of

$$\widehat{\boldsymbol{\Phi}}_{in} = \boldsymbol{S}_{in}\widehat{\boldsymbol{x}}_{in}. \quad [6]$$

In practice, the series is truncated, as the sensor array is not capable of characterising all possible harmonics. In fact, the number of basis vectors must be less than or equal to the number of channels (N_{chans}) in the array. This dimension is given as

$$N_{dims} = (L_{in}+1)^2 + (L_{out}+1)^2 - 2 \leq N_{chans} \quad [7]$$

where L_{in} and L_{out} are the truncation orders for the inner and outer subspaces, respectively. Cryogenic MEG systems contain c.300 channels, meaning high truncation orders are possible.

Further rejection of interference can be achieved by employing spatiotemporally extended SSS (tSSS). Perfect separation of sources is seldom achieved due to truncation and calibration errors (i.e. imprecise knowledge of the sensors' positions, orientations and gains). These errors result in 'mixing' of signals between the inner and outer subspaces [21]. A matrix intersection method can be used to identify signals existing in both the inner and outer signal vectors and, as the signals from the interference sources are likely to be stronger and correlated over longer time periods than brain activity, interference signals can be subtracted from the data. In practice, a correlation threshold, typically between 0.9 and 1.0, is used to determine whether a signal component is interference.

It has been shown previously that the triaxial construction of the OPMs used in this study produces arrays which have vastly improved interference rejection properties compared to single channel systems (e.g., SQUID-based sensors typically only measure a single component of magnetic field oriented approximately radially to the head surface) due to their ability to sample the full field vector [26], [27]. This extends, in principle, to an improved performance when the SSS method is applied, due to an improved ability to discriminate between internal and external sources. However, direct implementation of SSS as described above is challenging, as the lower channel count (here, 192-channels from 64 sensor positions) of OPM-MEG systems compared to cryogenic MEG scanners decreases the number of degrees of freedom in the model. This can make the inversion $\boldsymbol{S}^{+}$ unstable. Our previous work showed how an iterative approach to computing the pseudo-inverse matrix provides a stable computation of $\widehat{\boldsymbol{x}}_{in}$ by exploiting the hierarchical organisation of the SSS vectors to compute subsets of weights beginning with low order terms and iterating through to higher order harmonics [28]. This was shown to stabilise the solution in simulation but has yet to be applied (along with the spatiotemporal extension) to measured data.

D. Empty room noise recordings

To compare the MSRs, and investigate the performance of SSS and tSSS, we first performed empty-room noise recordings. The OPM helmet was placed at the approximate position of the head of a participant seated at the centre of the two MSRs. In MSR1, the room was demagnetised, and the on-sensor coils were used to zero the field around the OPMs prior to calibration using the manufacturer's software. Data were collected for 10-minutes. In MSR2, the background field was too strong for the on-sensor coils to cancel. To address this,

we constructed a triaxial square electromagnetic coil system to produce uniform fields equal and opposite to the field at the location of the helmet inside the shield. The coil (Fig.1(c)) was formed from three, co-centred square pairs of side length and separation 0.8 m with 6 turns, connected to a low-noise coil driver (QuSpin Inc.). The remanent field vector to be nulled was measured using a 'reference array' placed inside the helmet. The reference array comprised two orthogonally oriented second generation QuSpin ZFMs (dual axis, operating in 'field zeroing' mode and reporting fields of ±50 nT). The external coil currents were adjusted manually such that the reference sensors measured <1 nT along each coil axis. This coarse field nulling was enough for the on-sensor coils in the OPMs within the helmet to zero the background fields over the array. Once the OPMs were operational, 10-minutes of data were collected. The maximum recorded fields in this period for MSR1 and MSR2 were 0.38 nT and 1.44 nT, respectively.

All data were analysed using MATLAB (MathWorks Inc., Natick, Massachusetts, USA). For both datasets, first any channels which were inactive or showed excessive noise were manually removed (14 channels in MSR1 and 9 channels in MSR2). The power spectral density of the unprocessed data was then estimated by segmenting the data into 10 s chunks, computing a flat-top window and averaging across segments before plotting across the 0 – 100 Hz frequency band. Data were then processed with SSS, using the iterative approach, with 5 iterations with $L_{in} = 10$ and $L_{out} = 6$, and the PSD of the resulting $\widehat{\boldsymbol{\Phi}}_{in}$ was computed. Finally, tSSS was applied to the data in 10-s chunks using $L_{in} = 10$ and $L_{out} = 6$ and a correlation limit of 0.95. We hypothesised that the raw data collected in MSR1 would have a lower noise floor than data collected in MSR2. However, we expected that application of SSS and tSSS would have a larger effect in MSR2, and consequently help generate approximately equivalent empty-room noise spectra in the two rooms.

E. Phantom recordings

We investigated the impact of the level of shielding and the performance of SSS and tSSS on controlled signals generated inside the helmet by a dry-type current dipole phantom, which is an electromagnetic coil wound into an isosceles triangle (base 5 mm, height 45 mm) that mimics the spatial pattern of the magnetic fields produced by brain activity [29]. The phantom was placed inside the helmet and driven using a 16-bit NI-9264 (National Instruments, Austin, Texas, USA) voltage output source. The drive signal was generated using the MATLAB data acquisition toolbox, with an amplitude chosen such that the dipole moment was ~10 nAm and the maximum measured field would be <1,000 fT (to approximate neuromagnetic fields). A 100-ms burst of activity at 13 Hz was applied, followed by a 2 s rest period repeated 100 times. Trigger signals were used for precise timings. This experiment was repeated four times in each room. Between each run, the OPMs were re-zeroed and re-calibrated, the coil currents in MSR2 were adjusted between runs to compensate background field changes. Following removal of bad channels (12 channels in MSR1 and 9 channels in MSR2), channel and source level analyses were performed.

Channel level analysis: Data were first filtered between 1 and 40 Hz (Butterworth filter, 4th order) then segmented into trials using the trigger signal and averaged. The filtered data were also processed using SSS and tSSS (using the same parameters in the previous section) prior to segmentation and averaging. We expected that, regardless of the processing used, the phantom signal would be clearly identifiable in averaged data recorded in MSR1 but that SSS and tSSS would be required to identify the same signals in MSR2.

Source level analysis: We applied a linearly constrained minimum variance (LCMV) beamformer [30]. Briefly, an estimate of the current dipole source strength $\widehat{\mathbf{Q}}_{\boldsymbol{\theta}}(\mathrm{t})$, was formed at time t for dipole position and orientation $\boldsymbol{\theta}$ in a source space using a weighted sum of the measured data as

$$\widehat{\mathbf{Q}}_{\boldsymbol{\theta}}(\mathrm{t}) = \mathbf{w}_{\boldsymbol{\theta}}^{\mathrm{T}}\mathbf{m}(\mathrm{t}) \qquad [8]$$

where $\mathbf{m}(\mathrm{t})$ is a vector containing the magnetic field measurements recorded by all OPMs at time t and $\mathbf{w}_{\boldsymbol{\theta}}$ is a weights vector tuned to $\boldsymbol{\theta}$. The weights are chosen such that

$$\min\left[\widehat{\mathbf{Q}}_{\boldsymbol{\theta}}^2\right] \mathrm{s.t.}\, \mathbf{w}_{\boldsymbol{\theta}}^{\mathrm{T}}\mathrm{L}_{\boldsymbol{\theta}} = 1 \qquad [9]$$

where $\mathbf{L}_{\boldsymbol{\theta}}$ is the forward field vector containing the solutions to the MEG forward problem, i.e. the magnetic field pattern measured by the array from a unit current dipole at $\boldsymbol{\theta}$. The optimal weights vector is expressed as

$$\mathbf{w}_{\boldsymbol{\theta}}^{\mathrm{T}} = \left[\mathbf{L}_{\boldsymbol{\theta}}^{\mathrm{T}}\mathbf{C}^{-1}\mathbf{L}_{\boldsymbol{\theta}}\right]^{-1}\mathbf{L}_{\boldsymbol{\theta}}^{\mathrm{T}}\mathbf{C}^{-1} \qquad [10]$$

where $\mathbf{C}$ is the sensor data covariance matrix. The source space was a regular grid of 2 mm cubic voxels which span the volume of a 'template brain' which sits inside the helmet. The forward field vectors were calculated using a current dipole approximation inside a single-sphere conductor [31]. To regularise the covariance matrices, the Tikhonov method was employed, using 0.1% of the maximum singular value as the regularisation parameter. The source orientation was determined by generalised eigenvalue decomposition [32].

For each of the four datasets, we first filtered data between 1 and 40 Hz (using a 4$^{\mathrm{th}}$ order Butterworth filter). We then segmented data into trials of duration 0.4 s. These trials were concatenated, and this dataset was used to estimate the covariance matrices. We then estimated the change in electrical activity at each source location by constructing two covariance matrices for active and control periods, $\mathbf{C}_{\mathrm{a}}$ and $\mathbf{C}_{\mathrm{c}}$ respectively, and then calculating the pseudo-T-statistical contrast as

$$\mathrm{T}_{\boldsymbol{\theta}} = \frac{\mathbf{w}_{\boldsymbol{\theta}}^{\mathrm{T}}\mathbf{C}_{\mathrm{a}}\mathbf{w}_{\boldsymbol{\theta}} - \mathbf{w}_{\boldsymbol{\theta}}^{\mathrm{T}}\mathbf{C}_{\mathrm{c}}\mathbf{w}_{\boldsymbol{\theta}}}{2\mathbf{w}_{\boldsymbol{\theta}}^{\mathrm{T}}\mathbf{C}_{\mathrm{c}}\mathbf{w}_{\boldsymbol{\theta}}}. \qquad [11]$$

Pseudo-T-statistics were computed at the vertices of the 2 mm grid to produce an image of electrical activity. The active window was chosen to be 0 to 0.1 seconds (i.e. when the 13 Hz signal was on) and the control window was chosen to be 0.2 to 0.3 seconds (i.e. when no current was applied to the phantom). Following identification of the voxel at which the activation was a maximum, we computed an estimate of the timecourse of electrical activity at this peak voxel.

In addition, an estimate of the spatial specificity of the beamformer was made. We first computed the signal at the peak voxel, $\widehat{\mathbf{Q}}_{\boldsymbol{\theta}_{\mathrm{peak}}}(\mathrm{t})$ and then computed the correlation coefficient, r, between this 'peak' timecourse and the equivalent signal from nearby voxels, $\widehat{\mathbf{Q}}_{\boldsymbol{\theta}_{\mathrm{n}}}(\mathrm{t})$, (<5 cm from the

peak voxel). Plotting the values $r\left(\widehat{\mathbf{Q}}_{\boldsymbol{\theta}_{\mathbf{peak}}}(t), \widehat{\mathbf{Q}}_{\boldsymbol{\theta}_{\mathbf{n}}}(t)\right)^2$ as a function of the Euclidean distance from the peak voxel provides an estimate of spatial specificity, as the shared variance should decrease as distance to the peak voxel increases. To quantify this, we grouped distances into 2 mm bins, calculated the median within bins and took the mean and standard deviation of these values across the four runs before finding the smallest distance for which the median shared variance value was <50%.

The above analysis was repeated with covariance matrices calculated following the application of SSS and tSSS as described above. For MSR2, we expected that the application of SSS and tSSS prior to computation of the covariance matrix would increase the spatial specificity, as the level of noise suppression required from the beamformer would be reduced.

F. MEG demonstration

Finally, we performed a MEG recording to investigate whether OPM-MEG data could be collected in our lightly shielded environment. A single participant (male, 29) performed a motor task once in each room (with the helmet removed and replaced between runs). The study was approved by the University of Nottingham's Faculty of Medicine and Health Sciences Research Ethics Committee. The task required the participant to repeatedly abduct their right index finger following an auditory cue. Movement was sustained for 2 s until a second cue instructed the participant to stop. This was followed by a 3-s rest period and repeated for 100 trials. Experimental timings were controlled using MATLAB and a trigger signal was used to identify the onset time for each trial. We chose this task as it is known to robustly modulate beta (13-30 Hz) band oscillations in the contralateral sensorimotor cortex at the single participant level [33]. Specifically, from a right-hand finger abduction we expect to see a decrease in the amplitude of beta oscillations in the left sensorimotor area during the abduction period, with an increase in amplitude following movement cessation. Identification of the expected clear spatiotemporal signature of this induced effect in our data would thus indicate good (general) performance of both pre-processing and source reconstruction methods. In MSR2, the reference sensors required for field nulling were placed on top of the helmet. The participant was instructed to sit in a chair and remain still. Following removal of bad channels (10 channels in the MSR1 and 6 channels in MSR2), we conducted channel and source level analyses.

Channel level analysis: We computed time frequency spectra (TFS) showing the envelope of the amplitude of oscillations across frequency bands. This was generated by filtering data into overlapping frequency bands between 1 and 100 Hz, segmenting data into trials, computing the Hilbert envelope of the data and averaging across trials. To show relative change in beta amplitude, a contrast window of 4.6 – 4.8 s (relative to the initial cue) was chosen as baseline and the mean of the TFS in this window was subtracted before normalisation, to show change in amplitude relative to baseline. TFS were computed using the unprocessed data, and using data following application of SSS and tSSS. We expected that in MSR1, beta-band dynamics would be clear regardless of processing, but that SSS and tSSS would be needed to isolate the signal in MSR2.

Source level analysis: We again implemented a LCMV beamformer and performed a similar analysis to the phantom data. Here, the data were first filtered between 13 and 30 Hz (using a 4th order Butterworth filter) to tune the weights to the neural frequency of interest. A pseudo-T-statistical approach was again used to produce an image of beta modulation. The active window was chosen (from the sensor level analysis) to be 1 to 1.4 seconds following the onset cue (at 0 s) and the control window was chosen to be 2.8 to 3.2 seconds following the onset cue (cessation cue at 2 s). Following identification of the voxel at which the beta modulation was a maximum, we re-computed beamformer weights using broad-band (1-150 Hz) data covariance and calculated an estimate of the timecourse of electrophysiological activity at this peak voxel. A TFS of this signal was constructed in the same way as for channel level analysis. We also computed the spatial specificity estimate described above (using the beta-band derived virtual electrodes) again expecting to see an increase in spatial specificity when tSSS was applied to the data prior to beamforming.

III. RESULTS

A. Empty room noise recordings

Fig. 2(a) shows the median power spectral density computed across all channels for data collected in MSR1 (upper plot) and MSR2 (lower plot). Fig. 2(b) shows the corresponding frequency dependent shielding factor, computed as the ratio of the unprocessed PSD to the SSS- and tSSS-processed PSDs. The baseline noise level in MSR1 is ~15 fT/√Hz, which reduces to ~10 fT/√Hz following application of SSS and tSSS with shielding of 18 dB at 50 Hz and 50 dB at low frequency. MSR2 shows a raw noise level around an order of magnitude greater than MSR1. SSS achieves shielding of 18 dB at 50 Hz, whilst tSSS offers shielding of 55 dB at 50 Hz. The residual noise level of ~15 fT/√Hz following application of tSSS in MSR2 is a promising sign that MEG data can be isolated from noisy signals recorded in the light room.

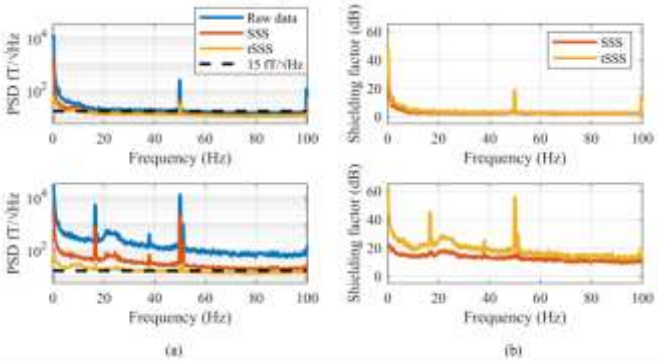

Fig. 2. Effects of SSS and tSSS on empty helmet OPM-MEG data collected in different environments. (a) shows noise spectra from MSR1 (top) and MSR2 (bottom). Blue, red and yellow lines show the median power spectral density across channels for unprocessed data, data pre-processed using SSS and data pre-processed using tSSS respectively. Black dashed line shows the 15 fT/√Hz target. (b) Shielding factor of SSS (red) and tSSS (yellow) as a function of frequency. tSSS produces a noise floor in MSR2 which is similar to MSR1.

B. Phantom recordings

Fig. 3(a) shows the trial averaged signals for all channels during one run of the phantom experiment in MSR1; upper, middle and lower panels show results for unprocessed data, data following SSS and data following tSSS, respectively. The ~400 fT amplitude response is clear after averaging with only a 1-40 Hz filter and remains similar when processed with SSS and tSSS. Fig. 3(b) shows the same plots for data recorded in MSR2, where the response is masked by noise in the filtered average. The response begins to emerge when SSS is applied, before being fully recovered by tSSS. Fig. 3(c) shows single-trial events from the tSSS-processed data recorded in MSR2. This demonstrates that low amplitude signals, around the level of a typical MEG response, can be isolated in a light MSR.

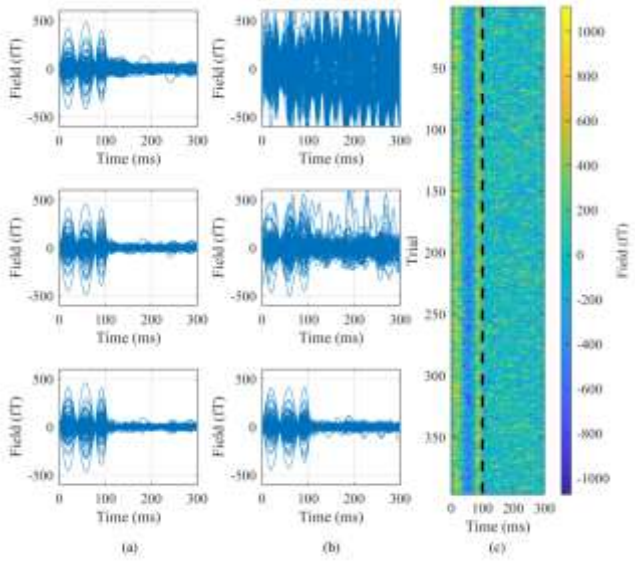

Fig. 3. Effects of tSSS on phantom data. (a) Data collected in MSR1 and (b) data collected in MSR2. For (a) and (b) the upper plot shows trial averaged phantom signals following 1-40 Hz bandpass filter. All channels have been overlaid. Middle plots show trial averaged phantom signal following SSS and lower plots show trial averaged phantom signal following tSSS. A clear response is produced in MSR1 in all cases, but processing with tSSS is needed to elicit the same clarity of response in MSR2. (c) Single trial responses from the channel with the highest absolute field, taken from data in MSR2 following tSSS. The black dashed line shows the time at which the phantom signal ended.

Fig. 4. compares the peak locations for the experiment. Fig. 4(a) left panel shows the helmet surface (shaded), along with the mean peak voxel location from MSR1. The mean position appears consistent regardless of the processing. The same plot for data collected in MSR2 is shown in the right panel. It displays less consistent peak voxel locations. Fig. 4(b) left and middle panels show, for MSR1 and MSR2 respectively, zoomed in views of 'error ellipsoids' for the mean locations. The centre of mass of the ellipsoids is the mean of the estimated locations across the four runs, and the size of the ellipsoid in each dimension represents the directional standard deviation across runs (the peak voxel for the tSSS processed data is the same in each run for MSR1 and so is shown as a single marker). Finally, Fig. 4(b) right panel shows the error ellipsoids for the results following pre-processing with tSSS in MSR2 and the single dot for MSR1, with overlap indicating good agreement between the localisations in the two MSRs.

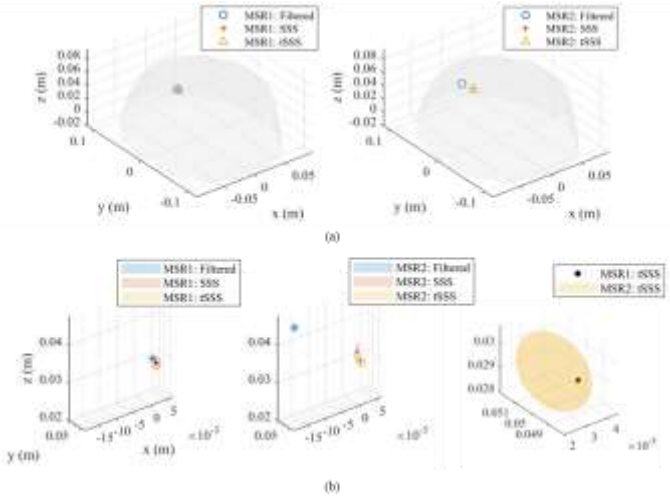

Fig. 4. Effects of tSSS on beamformer source localisation of phantom data. (a) Peak voxel positions relative to the OPM-MEG helmet (shaded surface) for four repeats of data collected in MSR1 (left plot) and MSR2 (right plot). The mean position across repeats is shown for the three analyses undertaken: following bandpass filtering only (blue circle), processing with SSS (red cross) and processing with tSSS (yellow triangle). In MSR1 the source localises to approximately the same peak voxel regardless of the processing applied, whereas in MSR2 the localisation is less consistent across processing methods. (b) shows zoomed in views of (a) on the left and centre plots with error ellipsoids indicating the standard deviation of the peak voxel across runs (tSSS processed datasets all localised to the same peak voxel for MSR1). The right-hand plot compares the results in both MSRs when processed with tSSS, the overlap indicating good agreement.

Fig. 5(a) shows the mean trial-averaged virtual electrode timecourse at the peak voxel for MSR1 with standard deviation across the four repeats shown using shaded error bars. Fig. 5(b) shows the same for MSR2. Recordings from MSR1 show similar amplitude signals around 12 nAm regardless of processing. In MSR2, the signal morphology is as expected, but the amplitude changes with processing, with tSSS yielding results closest to those from MSR1.

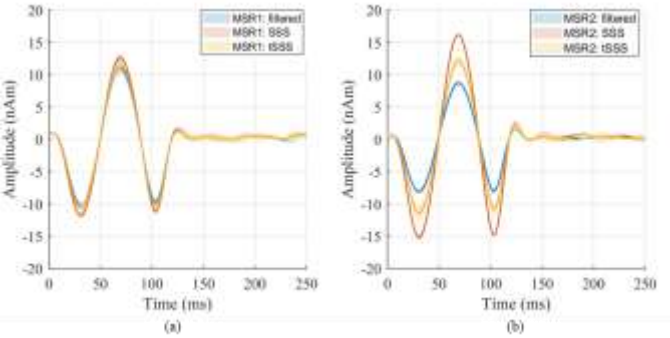

Fig. 5. Effects of tSSS on virtual electrode timecourses from peak voxel of beamformer source localization of phantom data. (a) Virtual electrodes averaged across four repeats with beamformer covariance computed from data recorded in in MSR1 following bandpass filtering only (blue), processing with SSS (red) and processing with tSSS (yellow). (b) Same results for data from MSR2. The morphology of the signal is maintained across conditions and MSRs, but the amplitude is altered in MSR2 without application of tSSS.

Fig. 6. shows the variation with distance of the shared variance of the virtual electrode timecourse at the voxel with the largest activation with the timecourses in nearby voxels. The mean over the four repeats of the median value across binned nearby voxels is plotted as a function of distance for

MSR1 (Fig. 6(a)) and MSR2 (Fig. 6(b)). The standard deviation across the four repeats is shown using shaded error bars. For MSR1, the slopes of the curves are approximately consistent regardless of pre-processing, and the point at which the median shared variance first becomes <50% is 1.8 cm, 1.6 cm and 1.6 cm for the 1-40 Hz filtered, SSS processed and tSSS processed data respectively. The corresponding distances for MSR2 are 2.6 cm, 2.6 cm and 1.6 cm, indicating that the spatial specificity of the beamformer is improved when SSS and tSSS are applied, bringing results in line with data collected in MSR1.

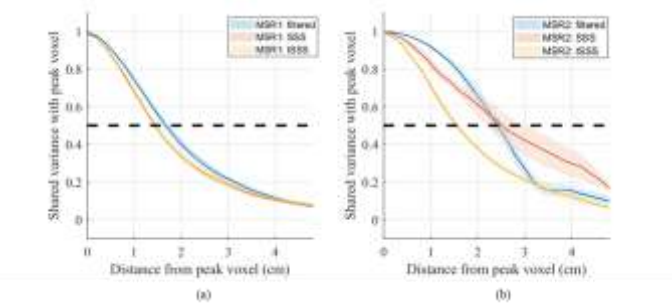

Fig. 6. Effects of tSSS on the spatial specificity of the beamformer during the phantom experiments. a) Data collected in MSR1 and b) data collected in MSR2. a) and b) both show the mean and standard deviation (as shaded error bars across the four repeats) of the median correlation between the time series of a virtual electrode at the peak of the beamformer image and virtual electrodes at nearby voxels. This is shown for data covariance computed following bandpass filtering only (blue), the SSS processed data (red) and the tSSS processed data (yellow). The application of tSSS increases the slope of the curves, this effect is more pronounced in MSR2. The black line shows the point at which the shared variance between voxels is 50%.

C. MEG demonstration

Fig. 7 shows channel-level analysis of MEG data. Fig. 7(a) shows TFSs for unprocessed data from MSR1 (upper panel) and MSR2 (lower panel). Fig. 7(b) and (c) show TFS for data pre-processed with SSS and with tSSS respectively. Results show that, regardless of processing, a similar response is obtained in MSR1, with the expected beta modulation clearly delineated, but that tSSS is needed to isolate the signal of interest from the noise at the channel level in MSR2. All results are shown for a single channel (sited over the left motor cortex) which produced the largest response in the unprocessed data in MSR1.

Fig. 8 shows source-level analysis of MEG data. The upper and lower panels of Fig. 6 show for data collected in MSR1 and MSR2 respectively. TFS for the (broad-band) virtual electrode time-series reconstructed at the source position with the largest contrast (in beta-band), using (a) unprocessed data, (b) data pre-processed with SSS and (c) data pre-processed with tSSS. Insets show pseudo-T-stat maps thresholded at 70% of the maximum value for each image, to illustrate the location and spatial extent of the activity. The beamformer successfully isolates the time-frequency response and localizes close to the expected region, regardless of the level of pre-processing. However, the activation images show a greater spatial extent without SSS or tSSS pre-processing.

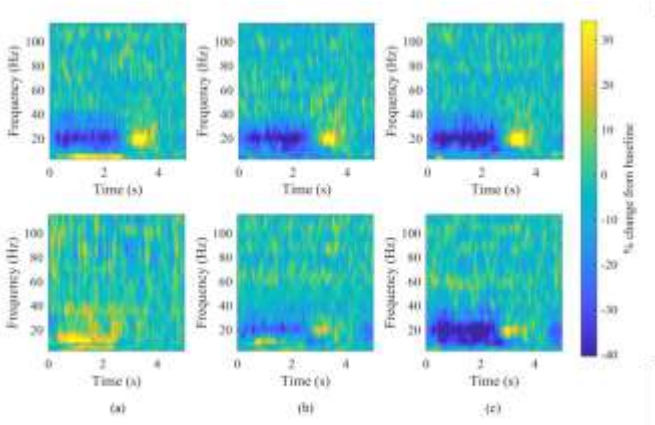

Fig. 7. Effects of SSS and tSSS on induced beta-band responses at the sensor level. (a) Time frequency spectra produced from unprocessed data from a single channel (placed over the left motor cortex, sensor chosen which had the highest signal strength in MSR1). Upper plot shows data from MSR1 and lower plots show data from MSR2. (b) TFS following SSS. (c) TFS following tSSS. In MSR1, the response is similar regardless of the processing step. In MSR2, SSS or tSSS is required to identify the beta band dynamics.

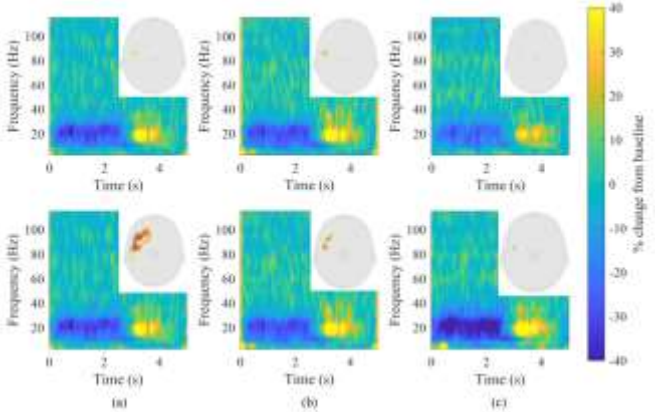

Fig. 8. Effects of SSS and tSSS on induced beta-band responses at the source level. (a) Time frequency spectra produced from an estimate of neuronal activity at the peak of a beamformer activation image. Upper plot shows data from MSR1 and lower plots show data from MSR2. (b) TFS following SSS. (c) TFS following tSSS. In both MSRs the shape and clarity of the temporal dynamics are similar regardless of the processing. Insets to each TFS show the pseudo-T-stat maps for each case, thresholded at 70% of the maximum pseudo-T-stat value. The spatial extent of the activation is greater in data from MSR2 indicating lower spatial specificity, which improves following tSSS.

Fig. 9(a) and 9(b) show for MSR1 and MSR2 respectively, the shared variance of the virtual electrode beta timecourse at the voxel with the largest beta modulation, with those reconstructed in other voxels, as a function of distance (note the similarity to Fig. 6 and phantom data). For MSR1, the slopes of the curves are approximately consistent regardless of pre-processing, and the point at which the median shared variance first becomes <50% is 1.4 cm, 1.2 cm and 1.0 cm for the beta-band filtered, SSS processed and tSSS processed data respectively. The corresponding distances for MSR2 are 3.2 cm, 1.8 cm and 1.6 cm, indicating spatial specificity of the beamformer is improved when SSS and tSSS are applied, bringing results in line with data collected in MSR1.

IV. Discussion

Our results show that both low amplitude signals from a brain-mimicking phantom, and motor induced modulation of

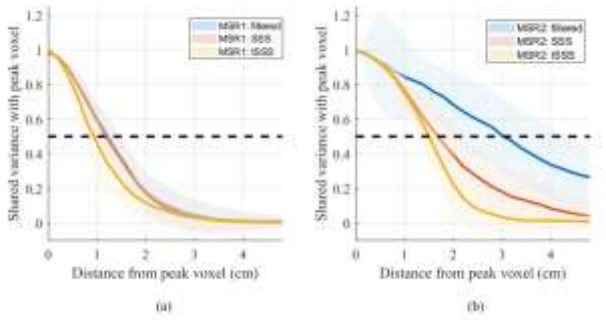

Fig. 9. Effects of tSSS on the spatial specificity of the beamformer. (a) Data collected in MSR1 (b) data collected in MSR2. Both show the median (solid line) and standard deviation (shaded area) of the shared variance between the time series of a virtual electrode at the peak of the beamformer contrast image and virtual electrodes at nearby voxels for the unprocessed data (blue), the SSS processed data (red) and the tSSS processed data (yellow). tSSS increases the slope of the curves, this effect is more pronounced in MSR2. The black dashed line shows the point at which the shared variance between voxels is 50%.

beta-band oscillations in a single participant can be accurately reconstructed from OPM-MEG data recorded in lightly shielded environments, by first applying active magnetic field cancellation with electromagnetic coils to enable OPM operation, and then applying the SSS and tSSS methods to remove interference. Despite the excellent noise rejection properties of a beamformer, pre-processing of data with tSSS improves the spatial specificity of the results both in the phantom data and in the MEG recording. Overall, these are important findings; previously, despite significant advances in sensor technology, a key drawback of OPM-MEG has been the need for costly and complicated magnetic shielding (beyond that which is required for conventional MEG). Here we demonstrate that such stringent shielding may not be necessary.

The effects of pre-processing data with SSS and tSSS prior to beamforming have been considered in conventional MEG analysis [34], typically noting little effect on spatial resolution [35] whereas direct integration of tSSS into a beamformer can improve spatial resolution in some cases [36]. Additionally, a light shield (constructed from a single shell of interleaved MuMetal and aluminium layers, with active compensation) for conventional MEG was shown to produce accurate localisations following tSSS [37]. However, further study of multiple subjects is required for OPM-MEG, where the use of multi-axis magnetometers instead of gradiometers leads to intrinsically noisier data; such study should also investigate less robust neural responses (i.e. beyond the beta-band modulation experiment performed here) to determine ultimate performance levels. We suggest that low SNR of data from MSR2 may lead to the flattening of the peak seen in the activation images [38] and that by rejecting noise prior to beamforming the contrast increases producing the positive effect in spatial specificity seen in our results.

Although critical for the collection of data in MSR2, the electromagnetic coil system we used here was primitive in design and enclosed the participant. Furthermore, we only compensated uniform magnetic field components and it is likely that field gradients were also present. We also did not compensate time-varying changes. Future studies should develop advanced coil systems for full field control and incorporate degaussing.

Future work should also investigate the effects of removing the conductive layer entirely, such that only a single layer of MuMetal remains. The eddy-current cancellation mechanism requires a material with a high electrical conductivity ($\sigma_{copper} = 5.8 \times 10^7$ S/m at 20°C) so that the induced current density is large enough to generate the magnetic shielding field. A second consideration is the skin-depth of the material, which for copper at 50 Hz is 9.2 mm. Although the thickness of the copper layers in MSR1 and MSR2 are 6 and 4 mm respectively, good shielding is possible as the eddy currents act over the large surface area of the copper layer, provided panels are in good electrical contact with one another [39]. In theory therefore, the shielding efficiency increases with shield size (whereas it decreases with increasing size for a high permeability shield). MuMetal does have relatively high electrical conductivity ($\sigma_{MuMetal} = 1.667 \times 10^6$ S/m) and along with its large relative permeability (10^4 – 10^5) the skin depth is much smaller in MuMetal than in copper. However, it is difficult to achieve these theoretically predicted increases in shielding efficiency with frequency in large MuMetal shields [39] because of the practicalities of maintaining current continuity and avoiding flux leakage in structures constructed using multiple panels.

The recent addition of the three-axis closed-loop operational mode to the OPMs used here is critical for deployment of OPM-MEG in magnetically challenging environments [24]. However, we note that despite the obvious advantages of working in this regime, closed-loop operation does not enable OPM operation if the residual background field is too strong, and data cannot be recorded if the field changes during an experiment exceed the sensors' working dynamic range. It also does nothing to reduce the impact of motion artefacts or environmental field changes on measured data. This means external coil systems are critical for OPM-MEG, especially if moving towards lighter shielded rooms.

The results reported here highlight the benefits of using signal space separation methods. In particular, the use of tSSS allows substantial separation of sources, aided by triaxial sensing. To illustrate, the mean angle between the inner and outer subspaces, which characterises the ability of the array to distinguish between internal and external sources, is around 60° for the 192-channel OPM-MEG used here, compared to around 10° for a commercial 306-channel SQUID-based system [20]. Despite expectation from the above that high levels of signal separation should occur for OPM-MEG from SSS alone, tSSS was required to fully reject the interference found in data recorded in MSR2. This is likely due to errors in the assumed geometry and calibration of the array, though calibration methods based on electromagnetic coils have been proposed to mitigate these effects [40].

It has also been proposed that spherical harmonics may not be the optimal choice of basis vectors when OPM arrays are placed nearer the scalp. Tierney et al. showed spherical harmonics poorly model activity in frontal and occipital brain regions, and demonstrated prolate spheroidal harmonics can better characterise signals in these cases [41]. Channel count is also critical, if the number of channels is close to the total

dimensions of the model, then unwanted amplification of noise occurs. We previously developed an iterative approach to SSS to mitigate this effect [28] (which was used to produce the data shown here) but Tierney et al. have proposed adaptive multipole modelling (AMM), which performs a projection orthogonal to the interference subspace [41]. This means fewer orders are required in the model, and AMM can be performed with fewer channels than were used here. Additionally, Wang et al. proposed optimising the origin and truncation order of SSS to maximise system SNR [42]. The above are all useful techniques for the present generation of OPM-MEG, but it is likely that channel count will continue to increase. Additional sensors should allow more conventional implementation of SSS.

V. Conclusion

We have shown that MEG data can be collected from OPM arrays operating inside lightly shielded environments. Empty-room noise recordings show comparable sensitivities to state-of-the-art OPM-optimised shields following application of tSSS. The tSSS method also allows for phantom signals to be clearly isolated in noisy recordings, and for a motor-induced beta-band modulation to be separated from interference sources during an OPM-MEG recording on a single participant. The use of lighter, cheaper and easier-to-site MSRs is critical for future success and widespread deployment of OPM-MEG.

Appendix: Dipole fit analysis of phantom data

As well as the beamformer analysis we also conducted a simple, single equivalent current dipole fit to estimate the position of the dipole phantom inside the helmet. The algorithm was implemented in MATLAB using the constrained minimisation algorithm ‘fmincon’ (optimisation toolbox) to maximise the correlation between measured fields and a model of the magnetic field for a current dipole inside a single sphere of uniform conductivity [31]. The search space was constrained inside the helmet. Localisation was performed separately for each run. We expected that (similar to the beamformer analysis) in MSR1, the localisation would be consistent regardless of processing, and that in MSR2 application of SSS and tSSS would improve localisation accuracy to a level comparable to MSR1. We also expected (from Fig. 3(b)) that the simple dipole fit localization accuracy may be poorer than the beamformer due to the lack of noise suppression in the algorithm.

Fig. A1. shows the dipole fit locations for each repeat of the experiment. Fig. A1(a) left panel shows the helmet surface (shaded), along with the estimated dipole locations from MSR1 displayed as ‘error ellipsoids’. The mean position and spatial extent of the ellipsoids in MSR1 appears consistent regardless of the level processing. The same plot for data collected in MSR2 is shown in the right panel. This shows greater variation in the fit locations prior to application of tSSS. Fig. A1(b) left and middle panels show zoomed in views of the error ellipsoids for MSR1 and MSR2 respectively. Finally, Fig. A1(b) right panel shows the error ellipsoids for the results following pre-processing with tSSS in MSR1 and MSR2 overlaid, with significant overlap indicating a high level of agreement between the localisations in the two MSRs.

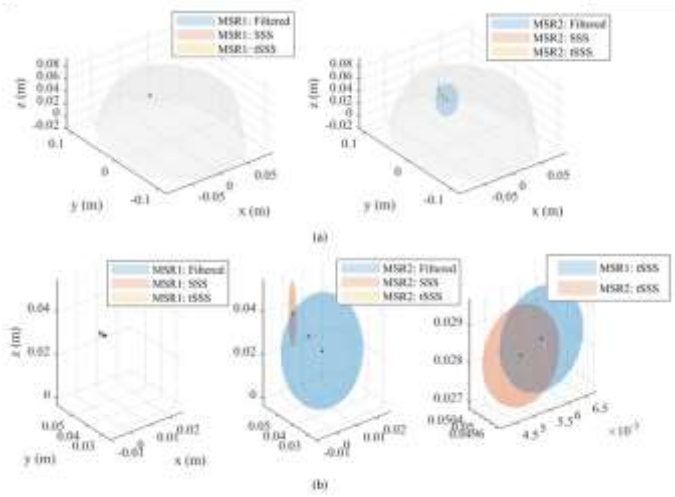

Fig. A1 Effects of tSSS on dipole fit of phantom data. (a) Dipole fit positions relative to the OPM-MEG helmet (shaded surface) for four repeats of data collected in MSR1 (left plot) and MSR2 (right plot). The mean and directional standard deviation across repeats are shown as error ellipsoids. Three error ellipsoids are shown for the three analyses undertaken: following bandpass filtering only (blue ellipsoid), processing with SSS (red ellipsoid) and processing with tSSS (yellow ellipsoid). In MSR1 the source localises to approximately the same position regardless of the processing, whereas in MSR2 the increase in the sizes of the blue and red ellipsoids indicate that localisation is less precise, unless tSSS is applied to the sensor level data. (b) shows a zoomed in view of (a) in the left and centre plots. The right-hand plot compares the error ellipsoids in both MSRs when processed with tSSS, the large overlap indicating good agreement between data.

Acknowledgment

We express our thanks to Isabel Brookes for assistance in constructing the coil system used in this work.

References

[1] M. Hämäläinen, R. Hari, R. J. Ilmoniemi, J. Knuutila, and O. V. Lounasmaa, “Magnetoencephalography theory, instrumentation, and applications to noninvasive studies of the working human brain,” *Rev. Mod. Phys.*, vol. 65, no. 2, pp. 413–497, 1993, doi: 10.1103/RevModPhys.65.413.

[2] S. Baillet, “Magnetoencephalography for brain electrophysiology and imaging,” *Nature Neuroscience*. 2017, doi: 10.1038/nn.4504.

[3] S. Rampp *et al.*, “Magnetoencephalography for epileptic focus localization in a series of 1000 cases,” *Brain*, vol. 142, no. 10, pp. 3059–3071, 2019, doi: 10.1093/brain/awz231.

[4] M. J. Brookes et al., “Magnetoencephalography with optically pumped magnetometers (OPM-MEG): the next generation of functional neuroimaging,” Trends Neurosci., vol. 45, no. 8, pp. 621–634, 2022, doi: 10.1016/j.tins.2022.05.008.

[5] H. Schofield *et al.*, “Quantum enabled functional neuroimaging: the why and how of magnetoencephalography using optically pumped magnetometers,” *Contemp. Phys.*, 2023, doi: 10.1080/00107514.2023.2182950.

[6] E. Boto *et al.*, “Moving magnetoencephalography towards real-world applications with a wearable system,” *Nature*, vol. 555, no. 7698, pp. 657–661, 2018, doi: 10.1038/nature26147.

[7] R. M. Hill *et al.*, “A tool for functional brain imaging with lifespan compliance,” *Nat. Commun.*, 2019, doi: 10.1038/s41467-019-12486-x.

[8] O. Feys *et al.*, “On-scalp magnetoencephalography for the diagnostic evaluation of epilepsy during infancy,” *Clin. Neurophysiol.*, vol. 155, pp. 29–31, 2023, doi: 10.1016/j.clinph.2023.08.010.

[9] L. Rier *et al.*, “The neurodevelopmental trajectory of beta band oscillations : an OPM-MEG study,” *bioRxiv*, 2024, [Online].

Available: https://doi.org/10.1101/2024.01.04.573933.
[10] N. Holmes *et al.*, “Enabling ambulatory movement in wearable magnetoencephalography with matrix coil active magnetic shielding,” *Neuroimage*, vol. 274, no. April, p. 120157, 2023, doi: 10.1016/j.neuroimage.2023.120157.
[11] S. Mellor *et al.*, “Real-time, model-based magnetic field correction for moving, wearable MEG,” *Neuroimage*, vol. 278, no. January, p. 120252, 2023, doi: 10.1016/j.neuroimage.2023.120252.
[12] N. Holmes *et al.*, “Naturalistic Hyperscanning with Wearable Magnetoencephalography,” *Sensors*, vol. 23, no. 12, 2023, doi: 10.3390/s23125454.
[13] J. C. Allred, R. N. Lyman, T. W. Kornack, and M. V. Romalis, “High-Sensitivity Atomic Magnetometer Unaffected by Spin-Exchange Relaxation,” *Phys. Rev. Lett.*, 2002, doi: 10.1103/physrevlett.89.130801.
[14] N. Holmes *et al.*, “OPEN A lightweight magnetically shielded room with active shielding,” *Sci. Rep.*, pp. 1–13, 2022, doi: 10.1038/s41598-022-17346-1.
[15] I. Altarev *et al.*, “Minimizing magnetic fields for precision experiments,” *J. Appl. Phys.*, 2015, doi: 10.1063/1.4922671.
[16] N. Holmes *et al.*, “A bi-planar coil system for nulling background magnetic fields in scalp mounted magnetoencephalography,” *Neuroimage*, 2018, doi: 10.1016/j.neuroimage.2018.07.028.
[17] J. Iivanainen, R. Zetter, M. Grön, K. Hakkarainen, and L. Parkkonen, “On-scalp MEG system utilizing an actively shielded array of optically-pumped magnetometers,” *Neuroimage*, 2019, doi: 10.1016/j.neuroimage.2019.03.022.
[18] A. Borna *et al.*, “A 20-channel magnetoencephalography system based on optically pumped magnetometers,” *Phys. Med. Biol.*, 2017, doi: 10.1088/1361-6560/aa93d1.
[19] S. Taulu and M. Kajola, “Presentation of electromagnetic multichannel data: The signal space separation method,” *J. Appl. Phys.*, vol. 97, no. 12, 2005, doi: 10.1063/1.1935742.
[20] S. Taulu, J. Simola, and M. Kajola, “Applications of the Signal Space Separation Method,” IEEE Trans. Sig. Proc., vol. 53, no. 9, pp. 3359–3372, 2005, doi: 10.1109/TSP.2005.853302.
[21] S. Taulu and J. Simola, “Spatiotemporal signal space separation method for rejecting nearby interference in MEG measurements,” *Phys. Med. Biol.*, vol. 51, no. 7, pp. 1759–1768, 2006, doi: 10.1088/0031-9155/51/7/008.
[22] N. Rhodes *et al.*, “NeuroImage Measurement of Frontal Midline Theta Oscillations using OPM-MEG,” *Neuroimage*, vol. 271, no. February, p. 120024, 2023, doi: 10.1016/j.neuroimage.2023.120024.
[23] M. Rea *et al.*, “Precision magnetic field modelling and control for wearable magnetoencephalography,” *Neuroimage*, vol. 241, no. June, p. 118401, 2021, doi: 10.1016/j.neuroimage.2021.118401.
[24] H. Schofield et al., “A Novel , Robust , and Portable Platform for Magnetoencephalography using Optically Pumped Magnetometers,” BioRxiv, 2024.
[25] A. Borna *et al.*, “Cross-Axis projection error in optically pumped magnetometers and its implication for magnetoencephalography systems,” *Neuroimage*, vol. 247, no. November 2021, p. 118818, 2022, doi: 10.1016/j.neuroimage.2021.118818.
[26] M. J. Brookes *et al.*, “Theoretical advantages of a triaxial optically pumped magnetometer magnetoencephalography system,” *Neuroimage*, vol. 236, no. March, p. 118025, 2021, doi: 10.1016/j.neuroimage.2021.118025.
[27] T. M. Tierney, S. Mellor, G. C. O’Neill, R. C. Timms, and G. R. Barnes, “Spherical harmonic based noise rejection and neuronal sampling with multi-axis OPMs,” *Neuroimage*, vol. 258, no. January, p. 119338, 2022, doi: 10.1016/j.neuroimage.2022.119338.
[28] N. Holmes, R. Bowtell, M. J. Brookes, and S. Taulu, “An Iterative Implementation of the Signal Space Separation Method for Magnetoencephalography Systems with Low Channel Counts,” *Sensors*, vol. 23, no. 14, 2023, doi: 10.3390/s23146537.
[29] D. Oyama, Y. Adachi, M. Yumoto, I. Hashimoto, and G. Uehara, “Dry phantom for magnetoencephalography -Configuration, calibration, and contribution,” *J. Neurosci. Methods*, vol. 251, pp. 24–36, 2015, doi: 10.1016/j.jneumeth.2015.05.004.
[30] J. Vrba and S. E. Robinson, “Signal processing in magnetoencephalography,” *Methods*, 2001, doi: 10.1006/meth.2001.1238.
[31] J. Sarvas, “Basic mathematical and electromagnetic concepts of the biomagnetic inverse problem,” *Phys. Med. Biol.*, vol. 32, no. 1, pp. 11–22, 1987, doi: 10.1088/0031-9155/32/1/004.
[32] K. Sekihara, S. S. Nagarajan, D. Poeppel, and A. Marantz, “Asymptotic SNR of scalar and vector minimum-variance beanformers for neuromagnetic source reconstruction,” *IEEE Trans. Biomed. Eng.*, vol. 51, no. 10, pp. 1726–1734, 2004, doi: 10.1109/TBME.2004.827926.
[33] G. Pfurtscheller and F. H. Lopes Da Silva, “Event-related EEG/MEG synchronization and desynchronization: Basic principles,” *Clinical Neurophysiology*. 1999, doi: 10.1016/S1388-2457(99)00141-8.
[34] A. Hillebrand, P. Fazio, J. C. de Munck, and B. W. van Dijk, “Feasibility of clinical Magnetoencephalography (MEG) functional mapping in the presence of dental artefacts,” *Clin. Neurophysiol.*, vol. 124, no. 1, pp. 107–113, 2013, doi: 10.1016/j.clinph.2012.06.013.
[35] A. Jaiswal *et al.*, “Comparison of beamformer implementations for MEG source localization,” *Neuroimage*, vol. 216, no. July 2020, p. 116797, 2020, doi: 10.1016/j.neuroimage.2020.116797.
[36] J. Vrba, S. Taulu, J. Nenonen, and A. Ahonen, “Signal space separation beamformer,” *Brain Topogr.*, vol. 23, no. 2, pp. 128–133, 2010, doi: 10.1007/s10548-009-0120-7.
[37] X. De Tiège *et al.*, “Recording epileptic activity with MEG in a light-weight magnetic shield,” *Epilepsy Res.*, vol. 82, no. 2–3, pp. 227–231, 2008, doi: 10.1016/j.eplepsyres.2008.08.011.
[38] A. Hillebrand and G. R. Barnes, “Practical constraints on estimation of source extent with MEG beamformers,” *Neuroimage*, vol. 54, no. 4, pp. 2732–2740, 2011, doi: 10.1016/j.neuroimage.2010.10.036.
[39] J. F. Hoburg, “Principles of Quasistatic Magnetic Shielding with Cylindrical and Spherical Shields,” *IEEE Transactions on Electromagnetic Compatibility*. 1995, doi: 10.1109/15.477342.
[40] J. Iivanainen *et al.*, “Calibration and Localization of Optically Pumped Magnetometers Using Electromagnetic Coils,” *Sensors*, vol. 22, no. 8, 2022, doi: 10.3390/s22083059.
[41] T. M. Tierney, G. R. Barnes, Z. Seedat, K. S. Pier, and S. Mellor, “Adaptive multipole models of optically pumped magnetometer data,” Human Brain Mapping, 45(4), 2024, doi: 10.1002/hbm.26596.
[42] R. Wang *et al.*, “Optimization of Signal Space Separation for Optically Pumped Magnetometer in Magnetoencephalography,” *Brain Topogr.*, vol. 36, no. 3, pp. 350–370, 2023, doi: 10.1007/s10548-023-00957-w.